

# Exploration of Effective Potential Landscapes using Coarse Reverse Integration

Thomas A. Frewen\*    Gerhard Hummer†    Ioannis G. Kevrekidis‡

July 18, 2021

## Abstract

We describe a reverse integration approach for the exploration of low-dimensional effective potential landscapes. Coarse reverse integration initialized on a ring of coarse states enables efficient “navigation” on the landscape terrain: escape from local effective potential wells, detection of saddle points, and identification of significant transition paths between wells. We consider several distinct ring evolution modes: backward stepping in time, solution arc-length, and effective potential. The performance of these approaches is illustrated for a deterministic problem where the energy landscape is known explicitly. Reverse ring integration is then applied to “noisy” problems where the ring integration routine serves as an outer “wrapper” around a forward-in-time inner simulator. Three versions of such inner simulators are considered: a system of stochastic differential equations, a Gillespie-type stochastic simulator, and a molecular dynamics simulator. In these “equation-free” computational illustrations, estimation techniques are applied to the results of short bursts of “inner” simulation to obtain the unavailable (in closed form) quantities (local drift and diffusion coefficient estimates) required for reverse ring integration; this naturally leads to approximations of the effective landscape.

---

\*Princeton University, Department of Chemical Engineering, Engineering Quadrangle, Olden Street, Princeton, NJ 08544; *e-mail*: [tfrewen@princeton.edu](mailto:tfrewen@princeton.edu).

†Laboratory of Chemical Physics, National Institute of Diabetes and Digestive and Kidney Diseases, National Institutes of Health, Bethesda, MD 20892-0520; *e-mail*: [Gerhard.Hummer@nih.gov](mailto:Gerhard.Hummer@nih.gov).

‡Princeton University, Department of Chemical Engineering, PACM and Mathematics, Engineering Quadrangle, Olden Street, Princeton, NJ 08544; *e-mail*: [yannis@princeton.edu](mailto:yannis@princeton.edu).

# 1 Introduction

When an energy landscape perspective is applicable, the dynamics of a complex system appear dominated by gradient-driven descent into energy wells, occasional trapping in deep minima, and transitions between minima via passage over saddle points through thermal “kicks”. A paradigm for this landscape picture is the trapping of protein configurations in metastable states en route to the dominant folded state. The underlying energy landscape is often likened to a roughened funnel with trapped states corresponding to local free energy minima<sup>1</sup>.

Important features on energy surfaces include local minima and their associated basins of attraction, saddle points, and minimum energy paths (MEPs) between neighboring minima passing through these saddles. Besides the identification of such landscape features, establishing the details of their connectivity is a task of considerable importance. Knowledge of the relative depths of landscape minima provides thermodynamic information. The kinetics of transitions between such states is determined by the type of “terrain” (smooth, rugged, etc.) that surrounds and separates them, in particular by the location and height of the low-lying saddles. The identification of important low energy molecular conformations in computational chemistry<sup>2</sup>, and determination of protein and peptide folding pathways<sup>3</sup>, to name but a few, rely on an ability to perform intelligent, targeted searches of the energy landscape.

Molecular dynamics (MD) and Monte Carlo (MC) simulations on energy landscapes are typically limited in the time scales they can explore by the difference between system thermal energy and the height of transitional energy barriers. A significant fraction of MD and MC simulation time is spent “bouncing around” in local minima. Energy barriers separating minima cause this type of trapping and the result is long waiting times between infrequent, but interesting, transition events. An array of techniques have been proposed to overcome such time scale limitations including bias-potential approaches<sup>4,5</sup>, accelerated dynamics<sup>6</sup>, coarse-variable dynamics<sup>7,8</sup>, and transition path sampling<sup>9,10</sup>, allowing extensive exploration

of the energy surface and its transition states. The adaptive bias force method<sup>11,12</sup> efficiently samples configurational space in the presence of high free energy barriers via estimation of the force exerted on the system along a well-defined reaction coordinate. Short bursts of appropriately initialized simulations are used in coarse-variable dynamics<sup>8</sup> to infer the deterministic and stochastic components of motion parametrized by an appropriate set of coarse variables. The use of a history-dependent bias potential in Ref. 13 ensures that minima are not revisited, allowing for efficient exploration of a free energy surface parametrized by a few coarse coordinates. Accelerated dynamics methods such as hyperdynamics and parallel replica dynamics<sup>6</sup> “stimulate” system trajectories trapped in local minima to find appropriate escape paths while preserving the relative escape probabilities to different states. Transition path sampling<sup>9</sup> generalizes importance sampling to trajectory space and requires no prior knowledge of a suitable reaction coordinate (see also transition interface sampling<sup>13</sup>).

Many energy landscape search methods have been devised (too numerous to discuss in detail here). “Single-ended” search approaches (where only the initial state is known) are based on eigenvector-following (mode-following)<sup>2,14,15,16,17,18</sup> and have been used to refine details of minimum energy paths (MEPs) close to saddle points<sup>19,20</sup>; methods purely for efficient saddle point identification also exist<sup>21,22,23</sup>. *Chain-of-state* methods are a more recent class of double-ended searches that evolve a chain of replicas (system states or “images”), distributed between initial and final states, in a concerted manner<sup>24</sup>. The original elastic band method<sup>25,26</sup> has been refined and extended many times<sup>27,28</sup>. More recently string methods<sup>29,30,31</sup>, which evolve smooth curves with intrinsic parametrization, have been used to locate significant paths between two states. The *Global Terrain* approach of Lucia and coworkers<sup>32,33</sup> exploits the inherent *connectedness* of stationary points along valleys and ridges on the landscape for their systematic identification.

We build here on the “equation-free” formalism of Ref. 35 whose purpose is to enable the performance of macroscopic tasks using appropriately designed computational experiments with microscopic models. The approach focuses on systems for which the coarse-grained,

effective evolution equations are assumed to exist but are not available in closed form. One example is the case of “legacy” or “black-box” codes, dynamic simulators which, given initial conditions, integrate forward in time over an interval  $\Delta t$ . Alternatively, the effective evolution equation for the system may be the unknown closure of a microscopic simulation model such as kinetic MC or MD. Rico-Martinez et al.<sup>34</sup> have used reverse integration in conjunction with microscopic *forward-in-time* simulators to access reverse time behavior of coarse variables (see also Ref. 37). Hummer and Kevrekidis<sup>8</sup> used coarse reverse integration to trace a *one-dimensional* effective free energy surface (and to escape from its minima) for alanine dipeptide in water. In this paper we use reverse integration in two dimensions: a ring of system initial states is evolved (forward in time in the “inner” simulation, and then reverse in the “outer”, coarse integration) to explore *two-dimensional* potential energy (and, ultimately, free energy) surfaces. The ring is evolved along the component of the local energy gradient (projected normal to the ring) while a nodal redistribution scheme is used that slides nodes along the ring so that they remain equidistributed in ring arclength, ensuring efficient sampling. Transformation of the independent variable in our basic ring evolution equation results in several distinct *stepping modes*.

The paper is organized as follows. In Section 2 we present our reverse ring integration approach. Ring evolution equations are developed with time, arc-length, or (effective) potential energy as the independent variable. We illustrate these stepping modes for a deterministic problem with a smooth energy landscape (Müller-Brown potential). In Section 3 reverse ring integration is investigated for three “noisy” problems: a system of stochastic differential equations (SDEs), a Gillespie-type stochastic simulation, and a molecular dynamics simulation of a protein fragment in water. Estimates of the quantities in the ring evolution equation are found by data processing of the results of appropriately initialized short bursts of the “black-box” inner simulator. The extension to stepping in free energy is discussed. We conclude with a brief discussion of the results and of the potential extension of the approach to more than two coarse dimensions.

## 2 Reverse integration on energy surfaces

Here we present a method for (low-dimensional) landscape exploration motivated by reverse projective integration, on the one hand, and by algorithms for the computation of (low-dimensional) stable manifolds of dynamical systems on the other. Reverse projective integration<sup>35</sup> uses short bursts of *forward in time* simulation of a dynamical system to estimate a local time derivative of the system variables, which is then used to take a large *reverse* projective time step via polynomial extrapolation. This type of computation is intended for problems with a large separation between many fast stable modes and a few (stable or unstable) slow ones; the long-term dynamics of the problem will then lie on an attracting, invariant “slow (sub)manifold”. Reverse projective integration allows us to compute “in the past”, approximating solutions *on this slow manifold* by only using the forward-in-time simulation code.

After each reverse projective step the reverse solution will be slightly “off manifold” (see Figure 1); the initial part of the next short forward burst will then bring the solution back close to the manifold, while the latter part of the burst will provide the time derivative estimate necessary for the next backward step. One clearly does not integrate the *full system* backward in time (the fast stable modes make this problem very ill-conditioned); it is the slow “on manifold” backward dynamics that we attempt to follow. The approach can be used for deterministic dynamical systems of the type described; however, it was developed having in mind problems arising in atomistic/stochastic simulation where the dynamic simulator is a molecular dynamics or kinetic Monte Carlo code. If the dynamics can be well described by a (low-dimensional) effective ODE, or an effective SDE, characterized by a potential (and by a (low-dimensional) effective free energy surface), reverse projective integration can be implemented as an “outer” algorithm, wrapped around the high-dimensional “inner” deterministic/stochastic simulator. The combination of short bursts of fine scale “inner” forward in time simulation with data processing and estimation and then with coarse-grained “outer” reverse integration can then be used to systematically explore these effective potentials (and

associated effective free-energy surfaces).

A natural set of protocols for such an exploration has already been developed (in the deterministic case) in dynamical systems theory – indeed, algorithms for the computation of low-dimensional *stable* manifolds of vectorfields provide the “wrappers” in our context (see the review in Ref. 38). This is easily seen in the context of a two-dimensional gradient dynamical system: an isolated local minimum of the associated potential is a stable fixed point and, locally, the entire plane is its stable manifold; the potential is a function of the points on this plane. In our 2-dimensional case, we approximate this stable manifold by a linearization in the neighborhood of the fixed point – this could be in the form of a ring of points surrounding the fixed point. One can then integrate the gradient vectorfield forward or backward in time (see Figure 2) keeping track of the evolution of this initial ring; using the gradient nature of the system, one can compute, as a byproduct, the potential profile.

Various versions of such “reverse ring integration” have been previously used for visualizing two-dimensional stable manifolds of vector fields. Johnson et al.<sup>36</sup> evolved a ring stepping in space-time arclength (see below) with empirical mesh adaptation and occasional addition of nodes to preserve ring resolution, building up a picture of the manifold as the ring expands. Guckenheimer and Worfolk<sup>37</sup> used algorithms based upon geodesic curve construction to evolve a circle of points according to the underlying vectorfield. A survey of methods for the computation of (un)stable manifolds of vectorfields can be found in Ref. 38, including approaches for the approximation of  $k$ -dimensional manifolds. In this paper we will restrict ourselves to the two-dimensional case (and thus, eventually, explore two-dimensional effective free energy surfaces).

Clearly, forward integration of our ring constructed based on local linearization around an isolated minimum, will generate a sequence of shrinking rings converging to the minimum (stable fixed point). For a two-dimensional gradient vectorfield, backward (reverse) ring integration will “grow” the ring – and as it grows on the plane, the potential on the ring evolves “uphill” in the initial well, possibly toward unstable (saddle-type) stationary points.

A critical issue in tracking the reverse evolution of such a ring is its distortion, as different portions of it evolve with different rates along the “stable manifold” (here, the plane). Dealing with the distortion of this closed curve and the deformation of an initially equidistributed mesh of discretization points on it requires careful consideration; similar problems arise, and are elegantly dealt with, in (forward in time) computations with the string method<sup>29,38</sup>. While we will first implement our reverse ring integration on a deterministic gradient problem (for descriptive clarity), our aim is to use it as a wrapper around atomistic/stochastic inner forward-in-time simulators; three such illustrations will follow.

## 2.1 The deterministic two-dimensional case

Consider a simple, two-dimensional gradient system of the form

$$\frac{d\mathbf{x}}{dt} = \begin{bmatrix} dx/dt \\ dy/dt \end{bmatrix} = -\nabla V(x, y). \quad (2.1)$$

In this case, since the vectorfield is explicitly available, with  $\mathbf{x}$  in  $\mathbb{R}^2$ , we can perform reverse integration by simply reversing the sign of the right hand side of equation (2.1); reverse *projective* integration will only become necessary in cases where the (effective) potential is not known, and the corresponding gradients need to be estimated from forward runs of a many-degree-of-freedom atomistic/stochastic simulator. Note also that here the dependent variables  $x$  and  $y$  are known (as are the corresponding evolution equations). For high dimensional problems with a low-dimensional *effective* description, selection of such good reduced variables (observables) is nontrivial; we will briefly return to this in the Discussion.

We start with a simple illustrative example: the Müller-Brown potential energy surface<sup>39</sup>, which is often used to evaluate landscape search methods since the minimum energy path (MEP) between its minima deviates significantly from the chord between them. We focus here on reverse ring evolution starting around a local minimum in the landscape and approaching the closest saddle point as the ring samples the well.

The potential is given by

$$V(x, y) = \sum_{i=1}^4 A_i \exp [a_i(x - x_i^0)^2 + b_i(x - x_i^0)(y - y_i^0) + c_i(y - y_i^0)^2] \quad (2.2)$$

where  $A = (-200, -100, -170, 15)$ ,  $a = (-1, -1, -6.5, 0.7)$ ,  $b = (0, 0, 11, 0.6)$ ,  $c = (-10, -10, -6.5, 0.7)$ ,  $x^0 = (1, 0, -0.5, -1)$ , and  $y^0 = (0, 0.5, 1.5, 1)$ . The neighborhood of the Müller-Brown potential we explore is shown in Figure 3 along with a listing of the fixed points, their energy, and their classification. We first discuss the initialization of the ring, and then three different forms of “backward stepping”: time-stepping, arclength-stepping in (phase space) $\times$ (time) and potential-stepping. Our initial ring will be the  $V = -105$  energy contour surrounding the minimum at  $(0.62, 0.03)$ .

A ring is a smooth curve  $\Phi$ , here in two dimensions. In our implementation, we discretize this curve and denote the instantaneous position of the discretized ring by the vectors  $\Phi_i \equiv \Phi(\alpha_i, t) = [x(\alpha_i, t), y(\alpha_i, t)]$  (with  $\Phi_i$  in  $\mathbb{R}^2$ ,  $\alpha_i$  in  $\mathbb{R}$ ) for the coordinates of the  $i^{\text{th}}$  discretization node, where  $\alpha_i$  is a suitable parametrization. A natural choice is the normalized arc-length along the ring with  $\alpha_i \in [0, 1]$ , as in the string method, but now with periodic boundary conditions. Note that one does not need to initialize on an exact isopotential contour; keeping the analogy with local stable manifolds of a dynamical system fixed point, one can use the local linearization – and more generally, local Taylor series – to approximate a closed curve on the manifold. Anticipating the “energy-stepping” reverse evolution mode, however, we start with an isopotential contour here. This requires an initial *point* on the surface; we then trace the isopotential contour passing through this point using a scheme which resembles the sliding stage in the “Step and Slide” method of Miron and Fichthorn<sup>22</sup> for saddle point identification. We simply “slide” along the contour to generate a curve  $\Gamma$ , moving (in some pseudo-time  $\tau$ ) perpendicular to the local energy gradient according to

$$\frac{d\Gamma}{d\tau} = \begin{bmatrix} \partial V / \partial y \\ -\partial V / \partial x \end{bmatrix}. \quad (2.3)$$



Points along the curve  $\Gamma$  provide initial conditions for ring nodes. Figure 4a illustrates ring initialization starting “in the well”, close to the isolated local minimum, resulting in a closed ring.

We note that our approach is closely related to established landscape search techniques based on following Hessian eigenvectors<sup>2,14,15,16,17,18</sup>; here the computation is performed in a dynamical systems setting: we use a dynamic simulator to estimate time derivatives (and through them local potential gradients) on demand.

## 2.2 Modes of Reverse Ring Evolution

### 2.2.1 Time Stepping

When every point on a curve evolves backward in time, it makes sense to consider the evolution of the entire curve in the direction of the component of the energy gradient normal to it (as also happens for forward time evolution in “string” methods, commonly used to identify minimum energy paths (MEPs)<sup>29</sup>). Ring nodal evolution is given by

$$\frac{d\Phi_i}{dt} = -(\nabla V(\Phi_i))^\perp + r\hat{T} \quad (2.4)$$

where  $\hat{T}$  is the unit tangent vector to  $\Phi$  at  $\Phi_i$ , with  $\hat{T} = \frac{\partial\Phi}{\partial\alpha}/|\frac{\partial\Phi}{\partial\alpha}|$  evaluated at  $\Phi_i$ , and  $r$  is a Lagrange multiplier field<sup>29</sup> (determined by the choice of ring parametrization) used to distribute nodes evenly along the ring. The component of potential gradient normal to the ring  $(\nabla V)^\perp$  is defined as follows

$$(\nabla V)^\perp = \nabla V - (\nabla V \cdot \hat{T})\hat{T} = \nabla V - (\nabla V)^\parallel \quad (2.5)$$

where  $(\nabla V)^\parallel$  is the component of the gradient parallel to the ring. For the general case where  $(\nabla V(\Phi_i))^\perp$  is unavailable in closed form (e.g. the inner integrator is a black-box timestepper) we use (multiple short replica) simulations for each discretization node on the ring to estimate

it, as will be discussed in Section 3. In practice, the tasks of node stepping and redistribution are often split into separate stages. The term involving  $r$  in equation (2.4) is first omitted, and nodal stepping is performed solving, backward in time, the  $N$ -node spatially discretized form

$$\frac{d\Phi_i}{dt} = F(\Phi_i, t) = -\nabla V(\Phi_i)^\perp, \quad i = 1, 2, \dots, N \quad (2.6)$$

where  $\Phi_i$  denotes the position of node  $i$  in the discretized ring. The normalized arc-length coordinate  $\alpha_i$  associated with the  $i^{\text{th}}$  node is approximated using the linear distance formula

$$\alpha_i = \frac{\sum_{j=1}^i \sqrt{(\Phi_j^x - \Phi_{j-1}^x)^2 + (\Phi_j^y - \Phi_{j-1}^y)^2}}{\sum_{j=1}^N \sqrt{(\Phi_j^x - \Phi_{j-1}^x)^2 + (\Phi_j^y - \Phi_{j-1}^y)^2}} \quad (2.7)$$

where  $(\Phi_i^x, \Phi_i^y)$  are the coordinates of node  $i$ . Periodicity of the ring (which has  $N - 2$  distinct nodes) is imposed by the set of algebraic equations

$$(\Phi_i)_t = (\Phi_{N-2+i})_t \quad (2.8)$$

where evaluation at time  $t$  is indicated by the subscript outside the parentheses. An explicit, backward in time, Euler discretization for the  $N - 2$  distinct nodes reads

$$(\Phi_i)_{t-\Delta t} = (\Phi_i)_t - \Delta t F(\Phi_i, t), \quad i = 2, 3, \dots, N - 1. \quad (2.9)$$

Backward stepping in time is followed by a redistribution step that slides nodes along the ring so that they are equally spaced (or, generally, spaced in a desirable manner) in the normalized ring arclength coordinate. These two basic steps are also present in the (phase space  $\times$  time) arclength or potential stepping of the ring discussed below; they are schematically summarized in Figure 5.

Figure 6 shows snapshots of the ring as it evolves backward in time – in the time-stepping mode – on the Müller-Brown potential. The ring quickly deviates from isopotential contours

as it climbs up the well. The local speed is proportional to the local component of the potential gradient normal to the ring; wide variation in nodal speeds causes the ring to evolve unevenly, elongating along the directions of steepest ascent. Initially equi-spaced ring nodes would, if not redistributed, rapidly converge towards regions of high potential gradients in our parametrization, resulting in poor resolution in other areas. Even the redistribution of nodes, however, will not suffice to accurately capture the ring shape as the ring perimeter quickly grows, unless new nodes are added.

### 2.2.2 Arc Length Stepping

Integration with respect to arclength in (phase) space  $\times$  time is a well known approach for problems where some of the dependent variables change rapidly with the independent variable (time). Johnson et al.<sup>36</sup> used this vector field rescaling to offset the concentration of flow lines in computing two-dimensional invariant manifolds of vectorfields whose fixed points have disparate eigenvalues. Ring evolution by integration along the solution arc  $s$  is used here by transformation of the independent variable for the system in equation (2.4). The required transformation relation<sup>40</sup> is

$$\left(\frac{dt}{ds}\right)_i = \left[1 + \left(\frac{d\Phi_i^x}{dt}\right)^2 + \left(\frac{d\Phi_i^y}{dt}\right)^2\right]^{-1/2} \equiv F_s(\Phi_i, t) \quad (2.10)$$

with coordinates  $(\Phi_i^x, \Phi_i^y)$  for node  $i$ . The transformed nodal evolution equation, with solution arclength as the independent variable, is given by

$$\frac{d\Phi_i}{ds} = \frac{d\Phi_i}{dt} \left(\frac{dt}{ds}\right)_i = F(\Phi_i, t)F_s(\Phi_i, t), \quad i = 2, 3, \dots, N - 1 \quad (2.11)$$

where  $F$  is as defined in equation (2.6), and the ring boundary conditions remain periodic.

In such an arc-length stepping mode, the ring evolution for our potential (Figure 7) is more robust to potential gradient nonuniformities. However, ring growth now does not couple to the topography of the landscape: in Figure 7b it “sags” along the  $y$ -direction and

there is considerable variation of potential values along any instantaneous ring state.

### 2.2.3 Potential Stepping

Evolving in constant potential steps enables the ring to directly track isopotential contours of the landscape. Potential stepping is shown schematically in one dimension in Figure 8 for a potential minimum bracketed by a sharp incline on one side and a more gradual one on the other. A (reverse) step in the potential results in small variations in the  $x$ -variable ( $(\Delta x)_1, (\Delta x)_2$ ) when the “terrain” is steep and in large  $x$  increments ( $(\Delta x)_3, (\Delta x)_4$ ) when it is shallow. A qualitatively different approach is that of Laio and Parinello<sup>41</sup> who employed a history-dependent bias as part of free energy surface searching that “fills” free energy wells; using repulsive markers actively prevents revisiting locations during further exploration. Irikura and Johnson<sup>42</sup> used a combination of steps parallel and perpendicular to the energy gradient in a version of isopotential searching to identify chemical reaction products from a reactant configuration.

Here we directly transform the independent variable of the evolution equations using the chain rule

$$\left(\frac{dt}{dV}\right)_i = \left[\frac{\partial V}{\partial \Phi_i^x} \frac{d\Phi_i^x}{dt} + \frac{\partial V}{\partial \Phi_i^y} \frac{d\Phi_i^y}{dt}\right]^{-1} \equiv F_V(\Phi_i, t) \quad (2.12)$$

so that, as long as the quantity above is finite (e.g. away from critical points), the ring evolution equations now become

$$\frac{d\Phi_i}{dV} = \frac{d\Phi_i}{dt} \left(\frac{dt}{dV}\right)_i = F(\Phi_i, t) F_V(\Phi_i, t), \quad i = 2, 3, \dots, N - 1. \quad (2.13)$$

Noting that  $F_V(\Phi_i, t) \rightarrow \infty$  in regions where the potential is “flat” ( $dV/dt \rightarrow 0$ ); we impose an upper limit on the change in the variables  $\Phi_i$  at each step of (2.13) when the threshold is exceeded.

Potential-stepping ring evolution on the Müller-Brown potential is shown in Figure 9: the ring efficiently rises within the well and successive rings are indicative of the topology of the

local landscape. The energy well is “sampled” evenly, tracking the potential contours. The almost linear segment of the ring visible in the final snapshot in Figure 9a is formed as the ring approaches the (stable manifold of the) saddle point on the potential at (0.21, 0.29); no further uphill motion, normal to the ring, is possible in this region. When such a situation is detected, one actively intervenes and modifies the evolution to assist the landscape search; examples of this will be given below.

## 2.3 Adjacent Basins

The reverse integration for the example in Section 2.2 consisted of initialization close to the bottom of a single well, ring evolution uphill, and approach to the neighboring saddle point. We now discuss a reasonable strategy for transitioning between neighboring energy wells.

Figure 10 shows the results of reverse ring integration for 3 different initial rings, one close to the bottom of each of the wells of the Müller-Brown potential. Reverse integration here maps out the basin of attraction of each of the wells. For each initial condition, the reverse integration “stalls” in the vicinity of neighboring saddle points and ring nodes “flow along” the stable manifold of the saddle. As the ring nodes approach a saddle point the component of the energy gradient normal to the ring ( $(\nabla V(\Phi_i))^\perp$ ) starts becoming negligible. To examine transitions between neighboring basins on the landscape we can employ *Global Terrain* methods<sup>32</sup> that exploit the inherent *connectedness* of stationary points along valleys and ridges on the landscape. Figure 11 indicates the basins of attraction for each of the minima (identified using reverse integration) along with a red curve, which connects *points that minimize the gradient norm along level curves of the potential* (a minimum energy path). This information is accumulated as the ring integration proceeds and suggests the direction to follow to locate neighboring minima. Upon detecting a local stagnation of ring evolution, caused by the approach to a saddle, a simple strategy is to (a) perform a local search for the saddle, through a fixed point algorithm, (b) compute the dynamically unstable eigenvector of this saddle, and (c) initialize a downhill search on the “other side” along this

eigenvector *away from the saddle point*. This search for the nearby minimum may be through simple forward simulation, or (in a global terrain context) by following points that minimize the gradient norm along level potential curves as above. This leads to the detection of a neighboring minimum, from which a new ring can be initialized and a further round of reverse integration performed. We reiterate that the procedure described so far (for purposes of easier exposition) is only for two-dimensional, deterministic landscapes.

### 3 Illustrative Problems for Effective Potential Surfaces

In this section we present coarse reverse integration using effective potential stepping for three “noisy” problems: a system of SDEs, a Gillespie-type stochastic simulation algorithm, and a molecular dynamics problem (alanine dipeptide in water). We assume that the problems we consider – in the regime we study them computationally – may be effectively modelled by the following bivariate Stochastic Differential Equation (SDE) (all the examples studied are effectively two-dimensional)

$$d\mathbf{X} = d \begin{bmatrix} X_1 \\ X_2 \end{bmatrix} = \begin{bmatrix} v_1(\mathbf{X}) \\ v_2(\mathbf{X}) \end{bmatrix} dt + \begin{bmatrix} D & 0 \\ 0 & D \end{bmatrix} d \begin{bmatrix} W_{1t} \\ W_{2t} \end{bmatrix} \quad (3.1)$$

where  $v_1(\mathbf{X})$  and  $v_2(\mathbf{X})$  are drift coefficients, the diffusion matrix  $\mathbf{D}$  is proportional to the unit matrix  $\delta_{ij}$  with  $\mathbf{D} = D\delta_{ij}$  (a “scalar” matrix), where  $D$  is a constant, and  $W_{1t}$  and  $W_{2t}$  are independent Wiener processes. We previously considered (Section 2.2) a deterministic example where numerical estimates for potential gradients were used to implement potential stepping. In the deterministic case, the drift coefficients are equal to minus the gradient of a potential  $V$ . For stochastic problems, such as those considered in this section, the drift coefficients are not so simply related to the gradient of an effective (generalized) potential (see the Appendix for additional discussion of this for 1-dimensional stochastic systems). In general, for reverse integration with steps in effective potential, we require estimates of all

drift coefficients and all entries in the diffusion matrix (and even their partial derivatives). Here we discuss effective potential stepping for a system of the form given in (3.1) and also briefly discuss the general case where entries of the diffusion matrix are non-zero and dependent on  $\mathbf{X}$ .

We assume equation (3.1) exists but is unavailable in closed form; estimates are therefore obtained by observing the process  $\mathbf{X}$  and using  $v_1(\mathbf{X}) \equiv \lim_{\Delta t \rightarrow 0} \langle [\Delta X_1] \rangle / \Delta t$ ,  $v_2(\mathbf{X}) \equiv \lim_{\Delta t \rightarrow 0} \langle [\Delta X_2] \rangle / \Delta t$ , and  $2D \equiv \lim_{\Delta t \rightarrow 0} \langle [\Delta X_1]^2 \rangle / \Delta t = \lim_{\Delta t \rightarrow 0} \langle [\Delta X_2]^2 \rangle / \Delta t$ . Here  $\Delta X_i = X_i(t + \Delta t) - X_i(t)$  and, by the form of equation (3.1),  $\lim_{\Delta t \rightarrow 0} \langle \Delta X_1 \Delta X_2 \rangle / \Delta t = 0$ .

These formulas, especially the ones for the drifts, suggest the construction of a useful coarse “pseudo-dynamical” evolution for our ring - a coarse evolution that follows the potential of mean force. The simplest version of these pseudo-dynamics evolves each point on the ring based on the local estimated drift - for the constant “scalar” diffusion mentioned above this evolution follows the potential of mean force (PMF), and it becomes a true dynamical evolution at the deterministic limit.

For a black box code implementing equation (3.1) this involves initializing at  $\mathbf{X}$ , running an ensemble of realizations of the dynamics for a short time  $\delta t$ , estimating the local drift components of the SDE using the above formulas, performing a (forward or backward) projective step  $\Delta t$  in time ( $\Delta X_i = v_i(\mathbf{X})\Delta t$ ), and repeating the process.

We will argue that this accelerated pseudo-dynamical evolution (which, we emphasize, does *not* correspond to realizations of the SDE itself) can assist in the exploration of effective potential surfaces. The easiest approach would be to use reverse time-stepping, or reverse arclength stepping in these pseudo-dynamics, and then (using formulae that will be discussed below and in the Appendix) finding the effective potential corresponding to each node visited. It is also possible, as we will see, to directly make “upward” steps in the effective potential; indeed, for the constant diffusion coefficient case we are studying, a proportionality exists between backward steps in time (for the pseudo-dynamics based on the drifts) and upward steps in the effective potential.

In the SDE case (Section 3.1) we only allow ourselves to observe sample paths generated by short bursts of the SDE solver; the SDE solver itself is treated as a black box (similarly for the Gillespie and MD simulators). A simple approach to estimating effective potential gradients (and eventually free energy gradients) is to perform sets of  $M$ -replica bursts of *inner* (SDE, Gillespie, MD) simulation initialized at each of the  $N$  ring nodes. For short replica simulation bursts (with  $n$  time steps), we can assume a local first order in time model<sup>43</sup> for the *mean*  $\bar{\mathbf{x}}$  (an  $n \times 2$  matrix, with entries averaged using multiple replicas, rows corresponding to time abscissas, and columns corresponding to each coarse variable)

$$\bar{\mathbf{x}} = \tilde{\mathbf{t}}\mathbf{C} + \boldsymbol{\epsilon} \quad (3.2)$$

where  $\tilde{\mathbf{t}} = [\mathbf{1} \ \mathbf{t}]$  is a  $n \times 2$  matrix,  $\mathbf{1}$  is a vector of  $n$  ones,  $\mathbf{t}$  is a vector of time abscissas,  $\boldsymbol{\epsilon}$  is the  $n \times 2$  matrix of model errors, and  $\mathbf{C}$  is the  $2 \times 2$  matrix of parameters computed (for each node) using least squares estimation. The (pseudo-time) derivative information (in the matrix  $\mathbf{C}$ ) is required, along with approximations of the tangent vectors at each node (ring geometry) to update the ring node positions in a reverse integration step; diffusion coefficients are also required, as discussed further below, to compute the relation between a reverse integration step size in pseudo-time and the corresponding change in the effective potential. In the remainder of the paper reverse ring time-stepping is always meant in terms of the drift-based pseudo-dynamics (it only becomes true time-stepping at the deterministic limit).

This derivative information may also be used to confirm the existence of an effective potential. For the case of two effective coarse-dimensions, we locally compare, computing on a stencil of points, the  $X_2$ -variation of  $dX_1/dt$  with the  $X_1$ -variation of  $dX_2/dt$  (testing for equality of mixed partial derivatives of the effective potential). Alternatively, we may use a



locally affine model for the drift coefficients of the following form

$$\begin{bmatrix} v_1(\mathbf{X}) \\ v_2(\mathbf{X}) \end{bmatrix} = \mathbf{A}\mathbf{X} + \mathbf{B} \quad (3.3)$$

with  $\mathbf{A} \in \mathbb{R}^{2 \times 2}$ ,  $\mathbf{B} \in \mathbb{R}^2$ , and employ maximum likelihood estimation techniques to compute  $\mathbf{A}$  and  $\mathbf{B}$  (an effective potential exists provided  $A_{12} = A_{21}$ ). In this context, recently developed maximum likelihood<sup>44</sup> or Bayesian<sup>45</sup> estimation approaches are particularly promising, allowing for simultaneous estimation of *both* the drift and diffusion coefficients. These approaches assume that the data are generated by a (multivariate) parametric diffusion; they employ a closed-form approximation to the transition density for this diffusion. For the case of a one-dimensional diffusion process  $\tilde{X}$

$$d\tilde{X} = \mu(\tilde{X}; \theta)dt + \sigma(\tilde{X}; \theta)dW_t \quad (3.4)$$

where  $W_t$  is the Wiener process,  $\theta$  is a parameter vector,  $\mu$  is the drift coefficient, and  $\sigma$  is the diffusion coefficient, the corresponding log likelihood function  $l_n(\theta)$  is defined as

$$l_n(\theta) = \sum_{i=1}^n \ln \left[ p_{\tilde{X}}(\Delta, \tilde{X}_{i\Delta} \mid \tilde{X}_{(i-1)\Delta}; \theta) \right] \quad (3.5)$$

where  $n$  is the number of time abscissas,  $\tilde{X}_{i\Delta}$  is the  $i^{\text{th}}$  sample, and  $\Delta$  is the time step between observations in the time series. The derivation of a closed-form expression for the transition density  $p_{\tilde{X}}$  (and thereby the log likelihood function) allows for maximization of  $l_n$  with respect to the parameter vector  $\theta$  providing “optimal” estimates for the drift and diffusion coefficients associated with the time series. For higher-dimensional problems (such as the two-dimensional ones considered here) see Ref. 48.

If the system in (3.1), with “scalar” diffusion matrix, has drift coefficients that satisfy

the following *potential condition*

$$\frac{\partial v_1(\mathbf{X})}{\partial X_2} = \frac{\partial v_2(\mathbf{X})}{\partial X_1} \quad (3.6)$$

it follows that the probability current vanishes at equilibrium, the drift coefficients (the time-derivatives in our ring pseudo-dynamics) satisfy

$$v_i = -D \frac{\partial(\beta E^{\text{eff}})}{\partial X_i}, \quad (3.7)$$

and the difference in effective generalized potential (free energy) between a reference state  $(X_1^0, X_2^0)$  and the state  $(X_1, X_2)$  may be directly computed from the following line integral<sup>46</sup>

$$\beta \Delta E^{\text{eff}} = -D^{-1} \left( \int_{X_1^0}^{X_1} v_1(X'_1, X_2^0) dX'_1 + \int_{X_2^0}^{X_2} v_2(X_1, X'_2) dX'_2 \right). \quad (3.8)$$

The analogy with the deterministic case (eqs.(2.12) and (2.13)) carries through: the estimated drifts are proportional (via the constant  $D$ ) to the effective potential gradients, and evolution following the drifts directly corresponds (modulo the proportionality constant) to evolution in the effective potential (PMF). Estimates of the local effective diffusion coefficients are typically necessary for exploration of the effective potential surface. We note that for a diagonal diffusion tensor with identical entries, (3.1), the size of the step  $\beta \Delta E^{\text{eff}}$  is scaled (in (3.8)) by the diffusion constant  $D$ . It follows that estimation of only the drift coefficients  $v_1(\mathbf{X})$  and  $v_2(\mathbf{X})$  allows us to perform reverse integration in our coarse dynamics (associated with the potential of mean force). A backward in time step  $\Delta t$ , leading to the state change  $\Delta X_i = v_i(\mathbf{X}) \Delta t$ , is, in effect, an “upward” step in the effective potential with the (unknown) scaled stepsize  $D \beta \Delta E^{\text{eff}}$ . This approach is analogous to (and, in the appropriate limit will approximate) the deterministic potential stepping previously described (Section 2.2). Here, for a stochastic problem, we need to additionally estimate diffusion coefficients to compute the potential change associated with each ring step uphill and, thereby,

the effective free energy change associated with each ring.

For the general diffusion matrix  $\mathbf{D}(\mathbf{X})$ , with all entries possibly non-zero and dependent on  $\mathbf{X}$ , we would compute the following partial derivatives of the effective potential

$$\begin{aligned} \frac{\partial(\beta E^{\text{eff}})}{\partial X_1} \equiv A_1 &= (\mathbf{D}(\mathbf{X}))_{11}^{-1} \left( \frac{\partial D_{11}}{\partial X_1} + \frac{\partial D_{12}}{\partial X_2} - v_1 \right) \\ &+ (\mathbf{D}(\mathbf{X}))_{12}^{-1} \left( \frac{\partial D_{21}}{\partial X_1} + \frac{\partial D_{22}}{\partial X_2} - v_2 \right) \end{aligned} \quad (3.9)$$

$$\begin{aligned} \frac{\partial(\beta E^{\text{eff}})}{\partial X_2} \equiv A_2 &= (\mathbf{D}(\mathbf{X}))_{21}^{-1} \left( \frac{\partial D_{11}}{\partial X_1} + \frac{\partial D_{12}}{\partial X_2} - v_1 \right) \\ &+ (\mathbf{D}(\mathbf{X}))_{22}^{-1} \left( \frac{\partial D_{21}}{\partial X_1} + \frac{\partial D_{22}}{\partial X_2} - v_2 \right) \end{aligned} \quad (3.10)$$

and test whether the following potential condition is satisfied<sup>46</sup>

$$\frac{\partial A_1(\mathbf{X})}{\partial X_2} = \frac{\partial A_2(\mathbf{X})}{\partial X_1}. \quad (3.11)$$

If these potential conditions are satisfied then the effective generalized potential (free energy) may again be directly calculated from the following line integral<sup>46</sup>

$$\beta E^{\text{eff}}(X_1, X_2) = \beta E^{\text{eff}}(X_1^0, X_2^0) + \int_{X_1^0}^{X_1} A_1(X_1', X_2^0) dX_1' + \int_{X_2^0}^{X_2} A_2(X_1, X_2') dX_2'. \quad (3.12)$$

We do not consider the case when equation (3.11) does not hold; we refer the reader to Ref. 49.

In the same spirit with reverse ring stepping in potential (Section 2.2), reverse ring stepping in effective potential may also be accomplished, subject to the stated assumptions, using the inner integrator as a black-box: we run multiple replicas for particular initial conditions (the positions of nodes in the ring), observe (inner) forward time evolution, and, for a “scalar” diffusion matrix, use the estimated drifts and (3.8) to approximate changes in the effective potential numerically. We note that for a constant and isotropic diffusion tensor if we estimate *only* the drift coefficients we can still perform reverse ring stepping

in the correct uphill direction and follow isopotential surfaces but the actual step size (and thus the actual value of the potential on the isopotential surfaces) will be unknown. As reverse ring integration proceeds, we store all calculated effective gradient values at each set of coarse variable values, thereby building a database. Smoothed gradient estimates may be obtained for each ring node by using a weighted gradient average that includes estimates at nearby coarse variable values in the database; we use kernel smoothing<sup>47</sup> to select appropriate weights. For the more general case of state-dependent diffusion the drift dynamics do not simply correspond to dynamics in the effective potential (see the Appendix for corrections to  $d\Phi_i/dt$  required to retain the analogy to the deterministic equations (2.12) and (2.13)). One could still employ the uncorrected drift dynamics as an *ad hoc* search tool (especially for problems close to “scalar” diffusion matrices) and post-compute the effective potential values the ring visits. In this case, however, the time-parametrization of the effective potential evolution will not be meaningful, and will even dramatically fail in the neighborhood of drift steady states that do not correspond to critical points in the effective potential (and vice versa).

### 3.1 A Stochastic Differential Equation Example

In this section we consider ring evolution in potential-stepping mode for a system of stochastic differential equations (SDEs). Reverse ring integration is performed at the *outer* level. The *inner* routine here is a forward-in-time SDE (Euler-Maruyama) integrator based on which we generate the nodal gradient estimates required by the outer ring integrator. The SDE system is given by

$$dx(t) = D_x F_x(t) dt + \sqrt{2D_x} dW_{1t} \quad (3.13)$$

$$dy(t) = D_y F_y(t) dt + \sqrt{2D_y} dW_{2t} \quad (3.14)$$

where  $D_x = D_y = D = 1$ ,  $F_x = -\frac{\partial V}{\partial x}$ ,  $F_y = -\frac{\partial V}{\partial y}$ , and the function  $V(x, y)$  is given by

$$V(x, y) = 10(x^2 - 1)^2 + 2x + \frac{1}{2}(y - x)^2. \quad (3.15)$$

The discretized (using the Euler-Maruyama scheme) system of equations is as follows

$$x(t + \Delta t) = x(t) + DF_x \Delta t + \sqrt{2D\Delta t} \mathcal{N}(0, 1) \quad (3.16)$$

$$y(t + \Delta t) = y(t) + DF_y \Delta t + \sqrt{2D\Delta t} \mathcal{N}(0, 1) \quad (3.17)$$

where  $\mathcal{N}(0, 1)$  is a normal random number with mean 0 and unit variance. We initialize the ring on an isopotential contour about the minimum at  $(-1.024, -1.024)$ . The ratio of eigenvalues at this fixed point is approximately 90 – the well is sharply elongated in the  $y$ -direction. To cope with this sharp elongation, we adaptively adjust the distribution of ring nodes so that they remain concentrated in regions where the ring curvature is largest (we did not adaptively change the number of nodes here).

The results of ring evolution (following drifts only) in a single well for the SDE problem are shown in the left panel of Figure 12 (contour lines are shown for  $V(x, y)$ ). Here we plot ring nodal positions at every reverse integration step in drift potential. Here, the selected diffusion coefficients ( $D_x = D_y = D = 1$ ) and the functional form of the drift and diffusion terms in eqs.(3.13) and (3.14) necessarily imply that  $\beta = 1$  – the effective potential is essentially the same as the drift potential (see also the Appendix). Reverse integration eventually stalls in the vicinity of the saddle point at  $(0, 0)$ . In Figure 12 (right panel) we show the estimated effective potential associated with ring nodes superimposed on 3D contour lines for  $V(x, y)$ . Estimates of both local drift and diffusion coefficients are used to compute effective potential differences (using equation (3.8)) for successive rounds of reverse integration (as generated by potential stepping, shown left). The effective potential is computed relative to that of the initial condition (a ring on an isopotential contour).

As the local curvature of the landscape changes, the duration of our short inner computation bursts (the time interval over which we collect data to estimate derivatives) should be adaptively modified for computational accuracy.

### 3.2 A Gillespie-type SSA inner simulator example

The stochastic description of a spatially homogeneous set of chemical reactions, which treats the collisions of species in the system as essentially random events, is based on the chemical master equation<sup>48</sup>. The Gillespie Stochastic Simulation Algorithm (SSA) is a Monte Carlo procedure used to simulate a stochastic formulation of chemical reaction dynamics that accounts for inherent system fluctuations and correlations – this procedure numerically simulates the stochastic process described by the spatially homogeneous master equation<sup>49</sup>. At each step in the simulation a reaction event is selected (based on the reaction probabilities), the species numbers updated (according to the stoichiometry of the reactions) and the time to the next reaction event computed. The reaction probabilities used in the algorithm are determined by the species concentrations and reaction rate constants as described in Ref. 52. The inner stochastic simulation routine we use here happens to employ an explicit tau-leaping scheme that takes larger time steps to encompass more reaction events while still ensuring that none of the propensity (reaction probability) functions in the algorithm changes significantly<sup>50</sup>. The reaction events we simulate are chosen to implement a mechanism which, at the limit of infinitely many particles, would be described by the deterministic gradient system with potential  $V(x, y)$  defined in equation (3.15).

Consider the following deterministic rate equations

$$\frac{dx}{dt} = -k_1x + k_2x^2 - k_3x^3 + k_4 - k_5x + k_6y \quad (3.18)$$

$$\frac{dy}{dt} = k_5x - k_6y + k_7. \quad (3.19)$$

This set of deterministic (coarse) rate equations may be written, for this problem, in the

form of the following gradient system

$$\frac{d\mathbf{x}}{dt} = -\nabla V^*(x, y) \quad (3.20)$$

where  $\mathbf{x}$  may be interpreted, here, as a vector of chemical species concentrations, and the potential energy function  $V^*(x, y)$  is given by

$$V^*(x, y) = \frac{(k_1 + k_5)}{2} x^2 - \frac{k_2}{3} x^3 + \frac{k_3}{4} x^4 - k_4 x - k_5 x y + \frac{k_6}{2} y^2 - k_7 y + k_8 \quad (3.21)$$

with

$$k_5 = k_6. \quad (3.22)$$

Values for the rate constants are selected by requiring  $V^*(x, y) = V(x - 5, y - 20)$  (i.e.  $V^*(x, y)$  is selected as a shifted version of the  $V(x, y)$  from the previous example, with its fixed points in the positive  $xy$  quadrant, in an attempt to enforce positivity of the reaction probabilities required by the Gillespie algorithm). The rate constant values chosen are  $k_1 = 2960, k_2 = 600, k_3 = 40, k_4 = 4783, k_5 = k_6 = 1, k_7 = 15$ . This models the following, hypothetical, set of elementary reactions



where species  $X$  (resp.  $Y$ ) has concentration  $x$  (resp.  $y$ ), the species  $T, U, V$ , and  $W$  are assumed to have unchanging concentration 1, and the reactions in eqs.(3.25) and (3.27) follow zeroth order kinetics.

For the number of particles used in this Gillespie simulation, the drift coefficients estimated from the simulation practically coincide with the right-hand-side of the *deterministic* rate equations, which happen to be embody the gradient of the *deterministic* potential  $V(x, y)$  (equation (3.15)). The results of reverse ring integration up this deterministic potential, with drifts estimated from our Gillespie simulation are shown in Figure 13. The left panel shows nodal evolution over 100 rounds of reverse integration. In the right panel we superimpose the nodal evolution (with estimated potential indicated by color) on contours of the potential  $V(x, y)$  (defined in equation (3.15)) for the deterministic gradient system in the form of (2.1). Since we are using an explicit tau-leaping Gillespie scheme, we do not have accurate estimates of the diffusion coefficients of the underlying chemical Fokker-Planck equation<sup>51</sup>. For this problem these entries in the diffusion matrix cannot be well approximated as state-independent, and a more involved process that includes their estimation is required in order to construct the true effective potential.

### 3.3 Alanine dipeptide in Water

In this section we study the coarse effective potential landscape of alanine dipeptide (i.e. *N*-acetyl alanine *N'*-methyl amide) dissolved in water using coarse reverse (effective potential-stepping) integration. This system is a basic fragment of protein backbones with two main torsion angle degrees of freedom  $\phi$  ( $C-N-C_\alpha-C$ ) and  $\psi$  ( $N-C_\alpha-C-N$ ), and with polar groups that interact strongly with each other and with the solvent. Extensive theoretical and experimental investigation of the alanine dipeptide has suggested good coarse observables (dihedral angles) for this system<sup>52,53,54</sup>.

Figure 14 shows the effective free energy landscape as a function of the dihedral angles  $\phi$  and  $\psi$  of the alanine dipeptide. The structures of the alanine dipeptide in the  $\alpha$ -helical ( $\psi = -0.3$ ) and extended ( $\psi = \pi$ ) states (corresponding to minima on the landscape) and at the transition state between them are also shown. We will use reverse integration on the effective potential energy landscape parametrized by these coarse coordinates. The



coarse reverse integration is “wrapped around” a conventional forward-in-time molecular dynamics (MD) simulator. It provides protocols for where (i.e. at what starting values of the coarse variables) to execute short bursts of MD, so as to map the main features of the effective potential surface (minima and connecting saddle points). These short bursts of appropriately initialized MD simulations provide (via estimation of the coefficients in equation (3.1)) the deterministic and stochastic components of the alanine dipeptide coarse dynamics parametrized by the selected coarse variables. The current work assumes a diffusion matrix (equation (3.1)) that is diagonal with identical constant entries. Our MD simulations of the alanine dipeptide in explicit water are performed using AMBER 6.0 and the parm94 force field. The system is simulated at constant volume corresponding to 1 bar pressure, and the temperature is maintained at 300K by weak coupling to a Berendsen thermostat. All simulations use a time step of 0.001 ps. The “true” effective potential here is the one obtained from the stationary probability distribution as approximated by a long MD simulation (24 ns).

A preparatory “lifting” step is required at each reverse integration step for each ring node. Each coarse initial condition is lifted to many microscopic copies conditioned on the coarse variables  $\phi$  and  $\psi$ . This step is not unique, since many distributions may be constructed having the same values of the coarse variables. Here we lift by performing a short MD run with an added potential  $V^{\text{constr}}$  that biases (as in umbrella sampling) the coarse variables towards their target values  $(\psi^{\text{targ}}, \phi^{\text{targ}})$ ,

$$V^{\text{constr}} = k_{\psi}(\psi - \psi^{\text{targ}})^2/2 + k_{\phi}(\phi - \phi^{\text{targ}})^2/2 \quad (3.28)$$

with  $k_{\psi} = k_{\phi} = 100 \text{ kcal mol}^{-1}\text{rad}^{-1}$ . The short lifting phase provides sufficient time for the fast variables to equilibrate following changes in the coarse variables. Following initialization we run and monitor the detailed MD simulations over short times (0.5ps) and estimate, for each node in the coarse variables, the local drifts over multiple replicas. Each coarse backward Euler step of the ring evolution provides new coarse variable values at which to initialize

short bursts of the MD simulator. Each step in the reverse integration procedure consists of lifting from coarse variables (the coordinates of the ring nodes) to an ensemble of consistent microscopic configurations, execution of multiple short MD runs from such configurations, restriction to coarse variables, estimation of coarse drifts and diffusivities, and reverse Euler stepping of the ring in the chosen evolution mode.

Figure 15 (left panel) shows ring nodes for 30 steps of reverse ring integration (using  $N=12$  nodes) initialized around the extended structure minimum. Successive rings evolve up the well and are representative of the well topology. Reverse integration stalls, as expected, at the saddle points neighboring the extended structure minimum and identifies candidate saddle points in these regions. We note that, in the current context of (assumed) constant diffusion coefficients we can think of these saddles as steady states of the set of deterministic ODEs, coinciding with the drift terms of the effective Fokker-Planck. Then the “dynamically unstable” directions in a saddle (the downhill ones) are characterized by *positive* eigenvalues of the *Jacobian* of the drift equations; yet since these equations are proportional to the negative of the gradient of a potential, positive eigenvalues of the dynamical Jacobian correspond to negative eigenvalues of the Hessian. The eigenvectors associated with the unstable (for our PMF-related coarse dynamics) eigenvalue at these candidate saddles are also indicated in Figure 15 and suggest the directions to dynamically follow to locate neighboring minima. We perturbed in the direction of the unstable eigenvector (associated with positive eigenvalue) away from one of the candidate saddle points and initialized (using a constrained potential, as before) multiple MD runs from this location. In Figure 15 (right panel) we plot the observed evolution from these initial conditions down into the basin of the adjacent  $\alpha$ -helical minimum.

In Figure 16 we show reverse ring evolution initialized close to both  $\alpha$ -helical and extended minima. Clearly reverse ring evolution in this  $\alpha$ -helical minimum well takes larger steps in  $\phi$ , in which direction the effective potential is shallowest. We repeat that the reverse integration steps correspond to constant steps in free energy only if the effective diffusion

tensor is diagonal and constant in both directions. The ring evolution shown in Figure 16 appears to accurately track equal free energy contours suggesting that these assumptions (on the form of the diffusion tensor) are a suitable approximation here.

## 4 Summary and Conclusions

We have presented a coarse-grained computational approach (coarse reverse integration) for exploration of low-dimensional effective landscapes. In our two-coarse-dimensional examples an (outer) integration scheme evolves a ring of replica simulations backwards by exploiting short bursts of a conventional forward-in-time (inner) simulator. The results of small periods of forward inner simulation are processed to enable large steps backward in time (pseudo-time in the stochastic case), in phase space  $\times$  time, or in potential in the outer integration. We first illustrated these different modes of reverse integration for smooth, deterministic landscapes. We extended the most promising approach for an illustrative deterministic problem, isopotential stepping, to relatively simple noisy (or effectively noisy) systems where closed-form evolution equations are not available. Simple estimation techniques were applied here to the results of appropriately initialized short bursts of forward simulation used locally to extract stochastic models with constant diffusion coefficients. Reverse integration in a single well and the approach to/detection of neighboring coarse saddles was demonstrated. A brief discussion of Global Terrain approaches for exploring potential surfaces was included, along with a short demonstration of linking our approach to them.

We have presented here ring exploration using an effective potential, using only estimation of the drift coefficients of our effective coarse model equations. Estimation of the diffusion coefficients (and their derivatives) is additionally required to quantitatively trace the effective potential surface. More sophisticated estimation techniques<sup>45,55</sup> allow for reliable estimation of both the stochastic and deterministic components of the coarse model equations. This permits a quantitative reconstruction of the effective free energy surface (and thereby the

equilibrium density) using our reverse integration approach. The latter reconstruction is possible provided that the potential conditions discussed in Section 3 hold; testing this hypothesis should become an integral part of the algorithm.

In studies of high-dimensional systems, a central question is the appropriate choice of coarse variables used in the reverse integration. For high-dimensional systems, such as those arising in molecular simulations, the dynamics can typically be monitored only along a few chosen “coarse” coordinates. Formally, an exact evolution equation can be derived for these coordinates with the help of the projection-operator formalism<sup>56</sup>, but that equation will be non-Markovian even if the time evolution in the full space is Markovian. To minimize the resulting memory effects, one can attempt to identify good (i.e., nearly Markovian) coordinates *a priori*, e.g., based on the extensive experience with the problem (as, say, in hydrodynamics) or by data analysis<sup>57,58</sup>. Alternatively, one can monitor the dynamics in a large space of trial coordinates and select a suitable low-dimensional space on the fly (e.g. from Principal Component Analysis<sup>59</sup>). In general problems, where good coordinates are not immediately obvious, careful testing of the Markovian character of the projected dynamics on the time scale of the coarse forward or reverse integration will be an important component of the computation<sup>58,60</sup>.

For the alanine dipeptide in water many-degree-of-freedom example, we assumed that the effective dynamics could be described in terms of a few coarse variables known from previous experience with the problem: the two dihedral angles. We are also exploring the use of diffusion map techniques<sup>61</sup> for data-based detection of such coarse observables, in effect trying to reconstruct Fig.0 without previous knowledge of the dihedral angle coarse variables. An example of mining large data sets from protein folding simulations to detect good coarse variables using a scaled Isomap (ScIMAP) approach can be found in Ref. 64; linking coarse variables with reverse integration for this example is discussed further in an upcoming publication<sup>62</sup>. All the work in this paper was in two coarse dimensions. In the context of invariant manifold computations for dynamical systems (which provided the motivation

for this work) more sophisticated algorithms exist for the computer-assisted exploration of higher-dimensional manifolds (as high as 6-dimensional)<sup>63,64</sup>. It should be possible – and interesting ! – to use these manifold parametrization and approximation techniques in combination with the approach presented here, to test the “coarse dimensionality” of effective free energy surfaces one can usefully explore.

**Acknowledgements.** This work was partially supported by DARPA and NSF (TAF and IGK) and by the Intramural Research Program of the NIDDK, NIH (GH).

# Appendix

## Stationary Probability Distribution and Effective Free Energy

We discuss here the effective potential (effective free energy  $E^{\text{eff}}(\psi)$ ) we attempt to compute through reverse integration and its relation to the form of the stationary probability distribution  $P_{st}(\psi)$  for a 1-dimensional Fokker Planck equation (FPE).

In 1-D we write the FPE (with drift

$$v(\psi_0) = \frac{\partial \langle \psi(t; \psi_0) \rangle}{\partial t} \quad (\text{A-1})$$

and diffusion coefficient

$$D(\psi_0) = \frac{1}{2} \frac{\partial \sigma^2(t; \psi_0)}{\partial t}, \quad (\text{A-2})$$

where  $\psi(t; \psi_0)$  is a sample path of duration  $t$  initialized at  $\psi_0$  when  $t = 0$  and where  $\sigma^2(\psi_0, t)$  is the variance of  $\psi(t; \psi_0)$  as follows:

$$\frac{\partial P(\psi, t)}{\partial t} = \left[ -\frac{\partial}{\partial \psi} v(\psi) + \frac{\partial^2}{\partial \psi^2} D(\psi) \right] P(\psi, t) = -\frac{\partial S(\psi, t)}{\partial \psi} \quad (\text{A-3})$$

where the probability current  $S(\psi, t)$  is given by

$$S(\psi, t) = v(\psi)P(\psi, t) - (\partial/\partial\psi)D(\psi)P(\psi, t). \quad (\text{A-4})$$

In 1-D, the stationary probability distribution corresponds to a constant probability current<sup>46</sup>; for natural boundary conditions this constant is zero and stationary solutions of the FPE satisfy

$$v(\psi)P_{st}(\psi) - (\partial/\partial\psi)D(\psi)P_{st}(\psi) = 0 \quad (\text{A-5})$$

which is readily solved for (the logarithm of)  $P_{st}$

$$\ln P_{st}(\psi) = -\ln D(\psi) + \int^{\psi} \frac{v(\psi')}{D(\psi')} d\psi' + const. \quad (\text{A-6})$$

The connection between the stationary probability distribution and the effective potential (effective free energy) for systems with a characteristic temperature/energy scale (given by the parameter  $\beta^{-1} = k_B T$ ), is provided by the ansatz  $P_{st}(\psi) \propto e^{-\beta E^{\text{eff}}(\psi)}$ . Substitution of the ansatz into eq.(A-6) gives

$$\beta E^{\text{eff}}(\psi) = \ln D(\psi) - \int^{\psi} \frac{v(\psi')}{D(\psi')} d\psi' + const.' \quad (\text{A-7})$$

In Section 3, after the fitting of model SDEs, we discussed the use of local estimates of the drift and diffusion coefficients in taking steps in some form of the effective potential for 3 example systems; we consider the basis of this approach here in 1-D. For both the SDE and Gillespie problems of Section 3 reverse ring stepping results were compared to particular deterministic potentials  $V(\psi)$  (eq.(3.15)). For the alanine dipeptide problem the results of reverse ring stepping were compared to an effective potential derived from the stationary probability distribution of the system (with the additional assumption of state-independent diffusion coefficients).

If, alternatively, we start from the Langevin equation

$$\ddot{\psi} = -\gamma(\psi)\dot{\psi} + f_0(\psi) + \Gamma(t). \quad (\text{A-8})$$

where  $\gamma(\psi)$  is the friction coefficient,  $f_0(\psi)$  is a deterministic force (minus the gradient of a deterministic potential function  $V(\psi)$ ),  $\gamma(\psi)\dot{\psi}$  is a drag force, and  $\Gamma(t)$  is the stochastic force, and take the high friction (overdamped) limit we obtain

$$\dot{\psi} = \frac{f_0(\psi)}{\gamma(\psi)} + \frac{\Gamma(t)}{\gamma(\psi)}. \quad (\text{A-9})$$

The fluctuation-dissipation relation connects (correlations of) the stochastic force to the drag

force as follows

$$\langle \Gamma(t)\Gamma(t + \tau) \rangle = \frac{2\gamma(\psi)\delta(t - \tau)}{\beta} \quad (\text{A-10})$$

for a system at “temperature”  $T$  (energy scale  $k_B T = \beta^{-1}$ ). Using Ito calculus we interpret eq.(A-9) as

$$d\psi = \frac{f_0(\psi)}{\gamma(\psi)} dt + \sqrt{\frac{2k_B T}{\gamma(\psi)}} dW_t \quad (\text{A-11})$$

with

$$v(\psi) \equiv \frac{f_0(\psi)}{\gamma(\psi)} = -\frac{1}{\gamma(\psi)} \frac{dV(\psi)}{d\psi} \quad (\text{A-12})$$

$$D(\psi) \equiv \frac{k_B T}{\gamma(\psi)} = \frac{1}{\beta\gamma(\psi)}. \quad (\text{A-13})$$

This establishes a correspondence of the Langevin equation with the FPE in eq.(A-3).

For the case of additive noise, where  $D(\psi) = D = \text{const}$  (implying (by eq.(A-13)) that  $\gamma(\psi) = \gamma = \text{const}$ ), we find (by differentiation of eq.(A-7) w.r.t.  $\psi$ ) that the drift coefficient  $v(\psi)$  is simply related to the effective potential  $E^{\text{eff}}$  as follows

$$v(\psi) \left( = \frac{d \langle \psi \rangle}{dt} \right) = -\frac{1}{\gamma} \frac{dE^{\text{eff}}(\psi)}{d\psi} = -D \frac{d(\beta E^{\text{eff}}(\psi))}{d\psi}. \quad (\text{A-14})$$

In this case, pseudo-dynamical reverse integration following drifts (as performed for the model SDE problem) coincides with stepping in effective potential (appropriately scaled with the constant diffusion coefficient). Using eq.(A-12) in eq.(A-15) we find

$$\frac{d(\beta V(\psi))}{d\psi} = \frac{d(\beta E^{\text{eff}}(\psi))}{d\psi} = -\frac{1}{D} \frac{d \langle \psi \rangle}{dt}. \quad (\text{A-15})$$

For the case of multiplicative (state-dependent) noise the drift coefficient  $v(\psi)$  is not directly related to the gradient of the effective potential  $E^{\text{eff}}$  extracted from the equilibrium



density; instead, it satisfies

$$v(\psi) \left( = \frac{d \langle \psi \rangle}{dt} \right) = -\frac{1}{\gamma(\psi)} \frac{d\hat{E}^{\text{eff}}(\psi)}{d\psi} = -D(\psi) \frac{d(\beta\hat{E}^{\text{eff}}(\psi))}{d\psi} \quad (\text{A-16})$$

where

$$\beta\hat{E}^{\text{eff}}(\psi) = -\int^{\psi} \frac{v(\psi')}{D(\psi')} d\psi' + \text{const.} \quad (\text{A-17})$$

with  $\beta\hat{E}^{\text{eff}}$  differing from  $\beta E^{\text{eff}}$  by the state-dependent contribution  $\ln D(\psi)$ . For such systems with state-dependent noise we require (local) estimates of *both* drift and diffusion coefficients for effective potential stepping. These can be used in eq.(A-7) (resp. eq.(A-17)) to compute (differences in) the true effective potential  $E^{\text{eff}}$  (resp. the “auxiliary” effective potential  $\hat{E}^{\text{eff}}$ )

$$\frac{d(\beta E^{\text{eff}}(\psi))}{d\psi} = -\frac{1}{D(\psi)} \frac{d \langle \psi \rangle}{dt} + \frac{1}{D(\psi)} \frac{dD(\psi)}{d\psi}. \quad (\text{A-18})$$

When temperature is not part of the problem description one considers the SDE

$$d\psi = A(\psi)dt + B(\psi)dW_t \quad (\text{A-19})$$

which has the following stationary distribution

$$P_{st}(\psi) = \frac{c}{B(\psi)} e^{\int^{\psi} \frac{A(\psi')}{B(\psi')} d\psi'}, \quad (\text{A-20})$$

$c$  being a normalization constant chosen such that  $\int_{-\infty}^{\infty} P_{st}(\psi') d\psi' = 1$ . Local estimates of  $A(\psi)$  and  $B(\psi)$  can then, in a similar approach as above, be used to step backwards in effective potential.

## References

- [1] P. G. Wolynes, J. N. Onuchic, and D. Thirumalai. *Science* **267**, 1619 (1995).
- [2] I. Kolossvary and W. C. Guida. *J. Am. Chem. Soc.* **118**, 5011 (1996).
- [3] C. L. Brooks, J. N. Onuchic, and D. J. Wales. *Science* (2001).
- [4] F. Wang and D. Landau. *Phys. Rev. Lett.* **86**, 2050 (2001).
- [5] T. Huber, A. Torda, and W. van Gunsteren. *J. Comput.* **8**, 695 (1994).
- [6] A. F. Voter, F. Montalenti, and T. C. Germann. *Annu. Rev. Mater. Res.* **32**, 321 (2002).
- [7] C. W. Gear, I. G. Kevrekidis, and C. Theodoropoulos. *Comp. Chem. Eng.* **26**, 941 (2002).
- [8] G. Hummer and I. G. Kevrekidis. *J. Chem Phys.* **118**, 23, 10762 (2003).
- [9] C. Dellago, P. G. Bolhuis, F. S. Csajka, and D. Chandler. *J. Chem. Phys.* **108**, 1964 (1998).
- [10] C. Dellago, P. G. Bolhuis, and D. Chandler. *J. Chem. Phys.* **108**, 9326 (1998).
- [11] E. Darve and A. Pohorille. *J. Chem. Phys.* **115**, 9169 (2001).
- [12] C. Chipot and J. Henin. *J. Chem. Phys.* **123**, 244906 (2005).
- [13] T. S. van Erp and P. G. Bolhuis. *J. Comp. Phys.* **205**, 157 (2005).
- [14] J. Baker. *J. Comput. Chem.* **7**, 385 (1986).
- [15] H. Taylor and J. Simons. *J. Phys. Chem.* **89**, 684 (1985).
- [16] C. J. Cerjan and W. H. Miller. *J. Chem. Phys.* **75**, 2800 (1981).
- [17] D. Poppinger. *Chem. Phys. Lett.* **34**, 550 (1975).

- [18] H. Goto. Chem. Phys. Lett. **292**, 254 (1998).
- [19] M. Page and J. McIver. J. Chem. Phys. **88**, 922 (1988).
- [20] C. Gonzalez and H. Schlegel. J. Chem. Phys. **95**, 5853 (1991).
- [21] I. V. Ionova and E. A. Carter. J. Chem. Phys. **98**, 6377 (1993).
- [22] R. A. Miron and K. A. Fichthorn. J. Chem. Phys. **115**, 19, 8742 (2001).
- [23] G. Henkelman and H. Jonsson. J. Chem. Phys. **111**, 15, 7010 (1999).
- [24] H. Jonsson, G. Mills, and K. W. Jacobsen. *Classical and Quantum Dynamics in Condensed Phase Simulations*. World Scientific, Singapore (1998).
- [25] R. Elber and M. Karplus. Chem. Phys. Lett. **139**, 375 (1987).
- [26] R. Gillilan and K. Wilson. J. Chem. Phys. **97**, 7757 (1992).
- [27] G. Henkelman, B. Uberuaga, and H. Jonsson. J. Chem. Phys. **113**, 22, 9901 (2000).
- [28] S. Trygubenko and D. Wales. J. Chem. Phys. **120**, 2082 (2004).
- [29] W. E, W. Ren, and E. Vanden-Eijnden. Phys. Rev. B **66**, 052301 (2002).
- [30] W. E, W. Ren, and E. Vanden-Eijnden. J. Phys. Chem. B **109**, 6688 (2005).
- [31] B. Peters, A. Heyden, A. Bell, and A. Chakraborty. J. Chem. Phys. **120**, 17, 7877 (2004).
- [32] A. Lucia, P. A. DiMaggio, and P. DePa. J. Global Optim. **29**, 297 (2004).
- [33] A. Lucia and F. Yang. Comp. Chem. Eng. **26**, 529 (2002).
- [34] R. Rico-Martinez, C. Gear, and I. Kevrekidis. J. Comp. Phys. **196**, 474 (2004).
- [35] C. W. Gear and I. G. Kevrekidis. Phys. Lett. A **321**, 335 (2004).

- [36] M. E. Johnson, M. Jolly, and I. G. Kevrekidis. *Num. Alg.* **14**, 125 (1997).
- [37] J. Guckenheimer and P. Worfolk. *Bifurcations and periodic orbits of vector fields*. Kluwer Academic (1993).
- [38] *W. Ren. Comm. Math. Sci.* **1**, 377 (2003).
- [39] K. Müller and L. D. Brown. *Theoret. Chim. Acta* **53**, 75 (1979).
- [40] M. Kubicek and M. Marek. *Computational Methods in Bifurcation Theory and Dissipative Structures*. Springer-Verlag (1983).
- [41] A. Laio and M. Parinello. *PNAS* **99**, 20, 12562 (2002).
- [42] K. Irikura and R. Johnson. *J. Phys. Chem. A.* **104**, 2191 (2000).
- [43] N. R. Draper and H. Smith. *Applied Regression Analysis*. Wiley series in probability and mathematical statistics. Wiley (1981).
- [44] Y. Ait-Sahalia. *Econometrica* **70**, 223 (2002).
- [45] G. Hummer. *New J. Phys.* **7**, 35 (2005).
- [46] H. Risken. *The Fokker-Planck Equation: Methods of Solutions and Applications*. Springer Series in Synergetics. Springer, 2nd edition (1996).
- [47] M. P. Wand. *Kernel smoothing*. Monographs on statistics and applied probability. Chapman and Hall (1995).
- [48] D. A. McQuarrie. *J. Appl. Prob.* **4**, 413 (1967).
- [49] D. Gillespie. *J. Phys. Chem.* **81**, 25, 2340 (1977).
- [50] D. Gillespie. *J. Chem. Phys.* **115**, 4, 1716 (2001).
- [51] Y. Cao, L. R. Petzold, M. Rathinam, and D. T. Gillespie. *J. Chem. Phys.* **121**, 12169 (2004).

- [52] P. J. Rossky and M. Karplus. *J. Am. Chem. Soc.* **101**, 1913 (1979).
- [53] C. L. Brooks and D. A. Case. *Chem. Rev.* **93**, 2487 (1993).
- [54] C. Chipot and A. Pohorille. *J. Phys. Chem. B* **102**, 281 (1998).
- [55] Y. Ait-Sahalia. Closed-form likelihood expansions for multivariate diffusions (2002). NBER Working Paper No. W8956. Available at SSRN: <http://ssrn.com/abstract=313657>.
- [56] R. Zwanzig. *Nonequilibrium Statistical Mechanics*. Oxford University Press (2001).
- [57] B. Nadler, S. Lafon, R. R. Coifman, and I. G. Kevrekidis. *Appl. Comput. Harmon. Anal.* **21**, 113 (2006).
- [58] R. B. Best and G. Hummer. *PNAS* **102**, 6732 (2005).
- [59] A. E. Garcia. *Phys. Rev. Lett.* **68**, 2696 (1992).
- [60] G. Hummer. *PNAS* **104**, 38, 14883 (2007).
- [61] R. Coifman, S. Lafon, A. Lee, M. Maggioni, B. Nadler, F. Warner, and S. Zucker. *PNAS* **102**, 7426 (2005).
- [62] P. Das, T. A. Frewen, I. G. Kevrekidis, and C. Clementi. In preparation (2007).
- [63] M. Henderson. *Int. J. Bifurcation and Chaos* **12**, 3, 451 (2002).
- [64] M. Henderson. *SIAM J. Appl. Dyn. Systems* **4**, 4, 832 (2005).

Figure 1. Schematic of reverse projective integration. The thick gray line indicates the position on the slow manifold as a function of time on a forward trajectory. The solid circles are configurations along microscopic trajectories run forward in time, as indicated by the short solid arrows. The long dashed arrows indicate the reverse projective steps, which result in an initialization near, but slightly off, the slow manifold.

Figure 2. Schematic of forward and backward stepping of ring nodes (light circles) in time on an energy landscape in the vicinity of fixed point (dark circles). Solid lines are energy contours, dashed lines connect ring nodes at each step, and arrows indicate the direction of the ring evolution.

Figure 3. Contour map of the Müller-Brown Potential for  $-1 < x < 1, -0.5 < y < 1$ . Contour lines are shown in black (white) for  $V(x, y) < 0$  ( $V(x, y) > 0$ ). Stationary points of the potential, their classification and energy are tabulated for the region illustrated.

Figure 4. Distribution of nodes produced by integration of equation (2.3) with initial condition above (white nodes and contour lines) and below (black nodes and contour lines) the saddle point energy. Below the saddle point there is a separation of isopotential contours in each well – the saddle point isopotential contours “split” in two.

Figure 5. Stages of ring evolution: backward stepping (in time  $\Delta t$ , arc-length  $\Delta s$ , or potential  $\Delta V$ ), followed by nodal redistribution.

Figure 6. Reverse time stepping on Müller-Brown Potential with  $\Delta t = 5 \times 10^{-5}, N = 80$  (successive rings are shown at intervals of 10 steps and arrows indicate direction of ring evolution).

Figure 7. Arc length stepping on Müller-Brown Potential with  $\Delta s = 0.01, N = 80$  (successive rings are shown at intervals of 10 steps and arrows indicate direction of ring evolution).

Figure 8. Energy stepping in a smooth, asymmetric 1D energy well.

Figure 9. Potential stepping on Müller-Brown Potential with  $\Delta V = 1.45$ ,  $N = 80$  (successive rings are shown at intervals of 10 steps and arrows indicate direction of ring evolution).

Figure 10. Potential stepping on the Müller-Brown Potential with  $\Delta V = 0.75$ ,  $N = 160$  (successive (colored) rings are shown at intervals of 10 steps). Successive rings obtained by reverse integration starting from each of the minima on the landscape are shown.

Figure 11. Potential stepping on Müller-Brown Potential with  $\Delta V = 0.75$ ,  $N = 160$  (successive (colored) rings are shown at intervals of 30 steps). Positions (red circles) of the minimum in gradient norm along the ring are shown at intervals of 5 steps in ring integration. Three different viewpoints of the same ring evolution are shown. Black arrows indicate the direction of ring evolution out of each minimum. Top row: 3D view; bottom row: 2D overhead view (gray arrows indicate position of views shown in top row).

Figure 12. Left: 100 rounds of potential-stepping ring evolution using coarse Euler and an inner SDE integrator with  $\Delta V = 5 \times 10^{-2}$ ,  $D = 1$ ,  $N = 200$ ; a redistribution that concentrates nodes in regions of largest ring curvature is performed every 10 reverse ring integration steps. The ring is initially centered at  $(-1, -1)$ . 50 replica runs are performed with the SDE integrator, each run for  $t_{tot} = 0.5$  (with time step size  $\Delta t = 2.5 \times 10^{-3}$ ), for drift estimation at each node. Contours of the function  $V(x, y)$  (defined in equation (3.15)) are shown. Ring nodes are shown for every step. Right: the effective potential associated with each ring node is shown (indicated by color) computed using local drifts and diffusions using (3.8) – it is plotted superimposed on the landscape of the potential (3.15). Evolving ring nodes with  $x < -1.2$  are omitted for clarity. Points on a single representative effective potential contour (using reverse drift-based integration) are plotted as black symbols in the  $V(x, y) = -10$  plane at the base of the figure; points along the actual potential contour are shown as red symbols.

Figure 13. Left: 100 rounds of drift potential-stepping ring evolution using an explicit tau-leaping inner Gillespie simulator with  $N = 200$ ; nodal redistribution is performed every 10 reverse ring integration (coarse Euler) steps. The ring is initially centered at  $(-1, -1)$ . 50 replica Gillespie simulation runs are performed, each run with 10,000 particles and the explicit tau leaping parameter  $\epsilon = 0.03$ . For the reverse integration  $\Delta V = 5 \times 10^{-2}$ . Contours of the function  $V(x, y)$  (defined in equation (3.15)) are shown. Right: 3D-view of reverse ring integration shown left with estimated potential of each node shown in color. Colorbar indicates value of  $V(x, y)$ . Evolving ring nodes with  $x < -1.2$  are omitted for clarity. Contours of the function  $V(x, y)$  (defined in equation (3.15)) are shown in 3D. Points on a single representative potential contour (as computed using reverse integration) are plotted as black symbols in the  $V(x, y) = -10$  plane at the base of the figure; points along the actual potential contour are shown as red symbols.

Figure 14. Free energy landscape for the alanine dipeptide in the  $\phi - \psi$  plane ( $1k_B T$  contour lines). Structures are shown corresponding to the right-handed  $\alpha$ -helical minimum (left), the extended minimum (right), and the transition state between them (middle).

Figure 15. Alanine dipeptide ring integration. Left panel: Extended structure minimum: 30 rounds of reverse (coarse Euler) ring integration (number of ring nodes  $N=12$ ) with scaled effective potential steps. Note that the scaled steps correspond to constant steps in free energy only if the effective diffusion tensor is diagonal with identical, constant entries, which appears to be a good approximation here. Eigenvectors corresponding to positive eigenvalues for candidate saddle points determined from ring integration are shown (long red arrows). Right panel: Downhill runs initialized at transition regions suggested by the reverse ring integration from the extended structure minimum. Initial conditions (black dots) are generated by umbrella sampling at a target coarse point selected by perturbation along the unstable eigenvector at the saddle. Final conditions for these downhill runs (purple dots) suggest starting points for a new round of reverse integration from the adjacent minimum.



( $1k_B T$  contour lines used in both plots). Note that both wells are plotted rotated by 90 degrees relative to Figure 14.

Figure 16. Alanine dipeptide in water: 30 rounds of coarse reverse ring evolution (number of ring nodes  $N=12$ ,  $D\beta\Delta E^{\text{eff}} = 0.05k_B T$ ) initialized in the neighborhood of both the right-handed  $\alpha$ -helical minimum (bottom ring), and the extended minimum (top ring). Rings (grey lines) connecting nodes (black solid circles) are shown. Colored energy contours are plotted at increments of  $1k_B T$ .

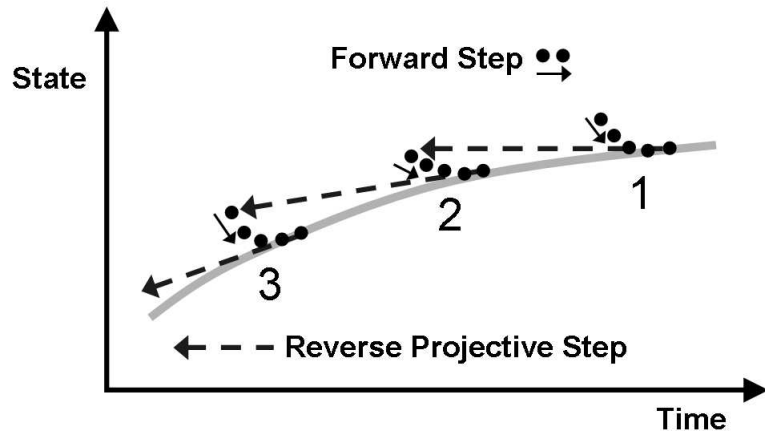


Figure 1

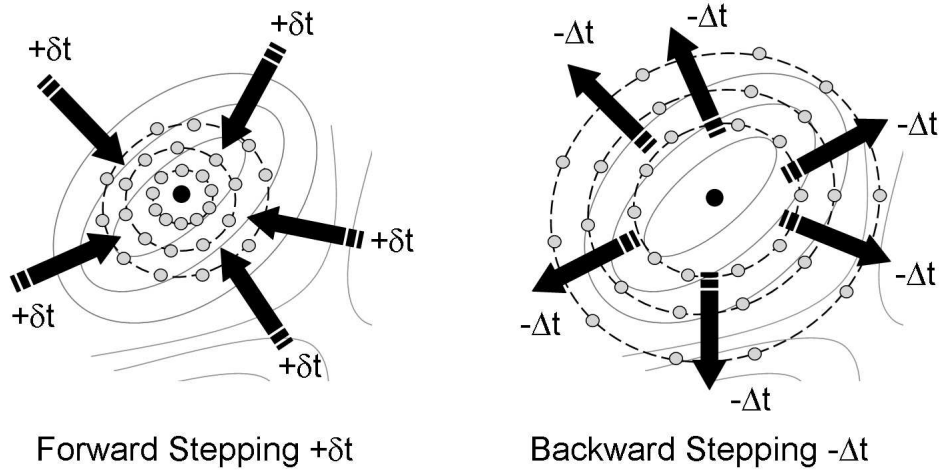
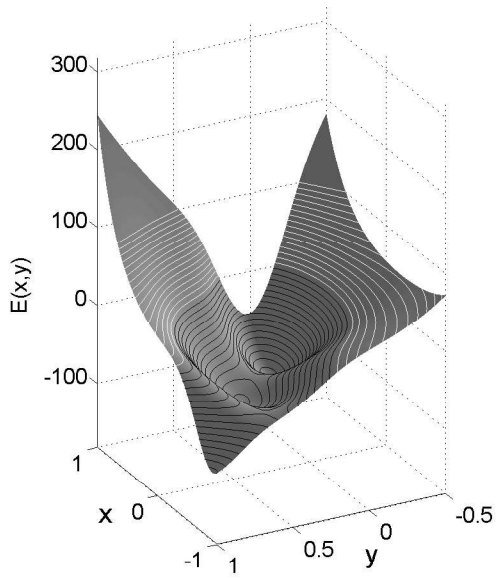


Figure 2



| $x$   | $y$  | $V(x,y)$ | <i>Feature</i> |
|-------|------|----------|----------------|
| 0.62  | 0.03 | -108.2   | Minimum        |
| -0.05 | 0.47 | -80.8    | Minimum        |
| -0.82 | 0.62 | -40.7    | Saddle Point   |
| 0.21  | 0.29 | -72.2    | Saddle Point   |

Figure 3

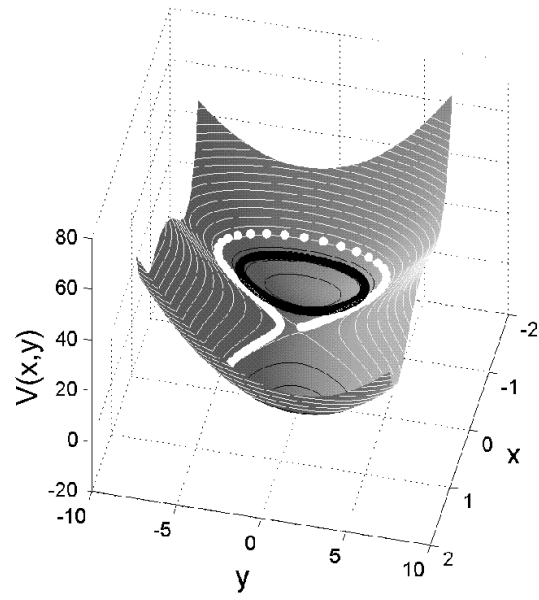
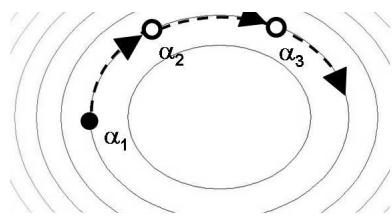


Figure 4

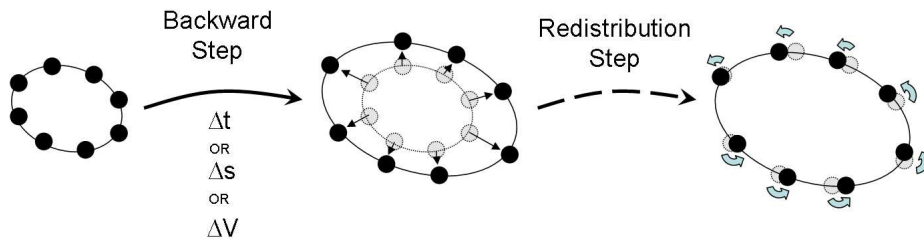


Figure 5

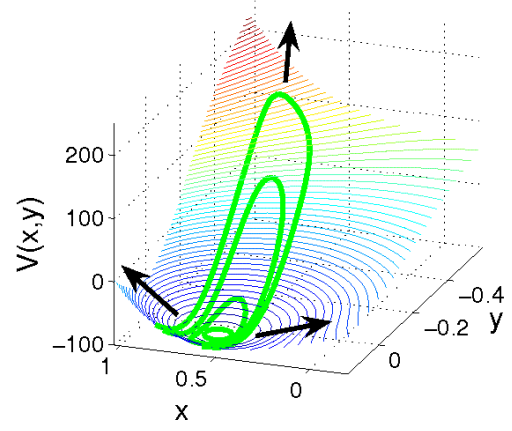
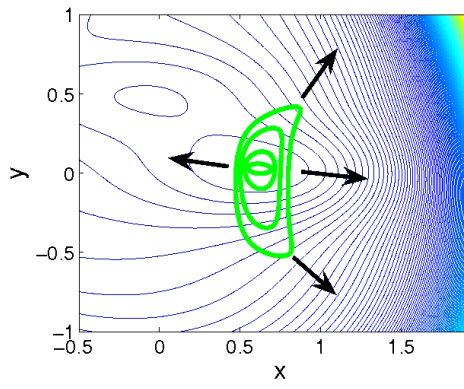


Figure 6

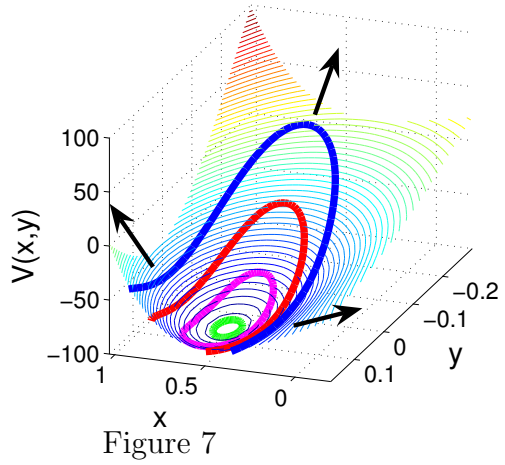
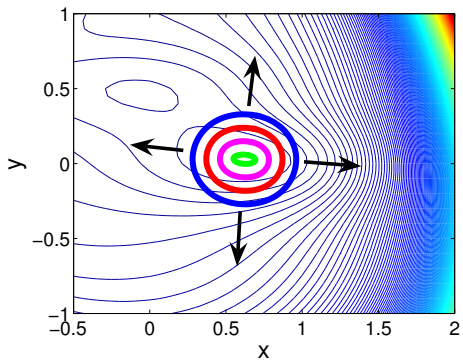


Figure 7



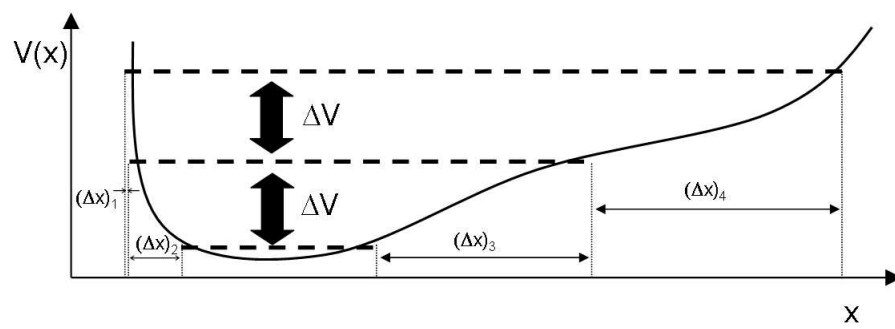


Figure 8

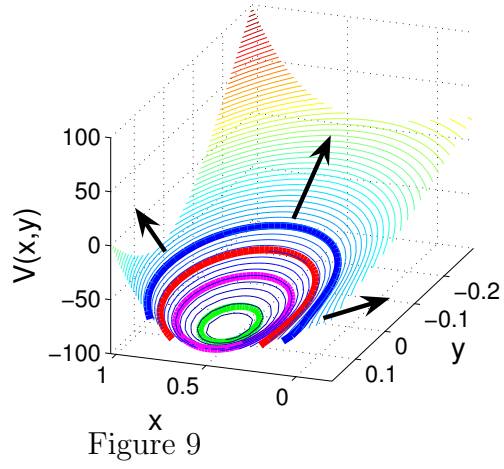
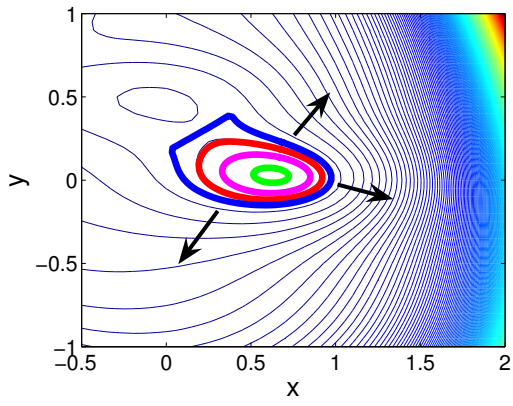


Figure 9

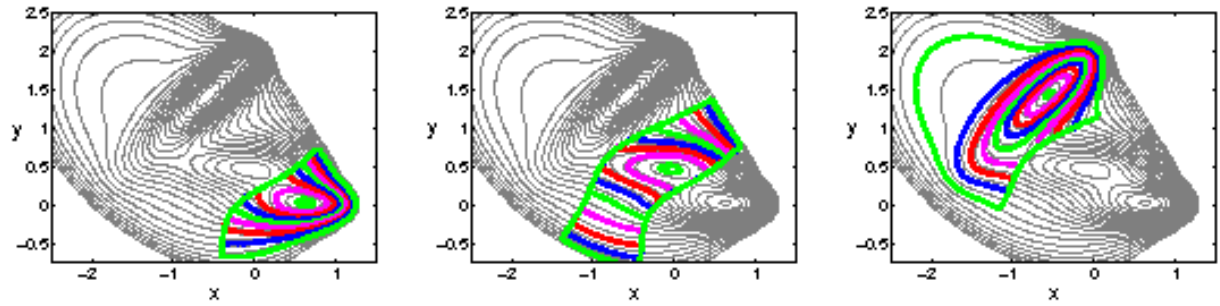


Figure 10

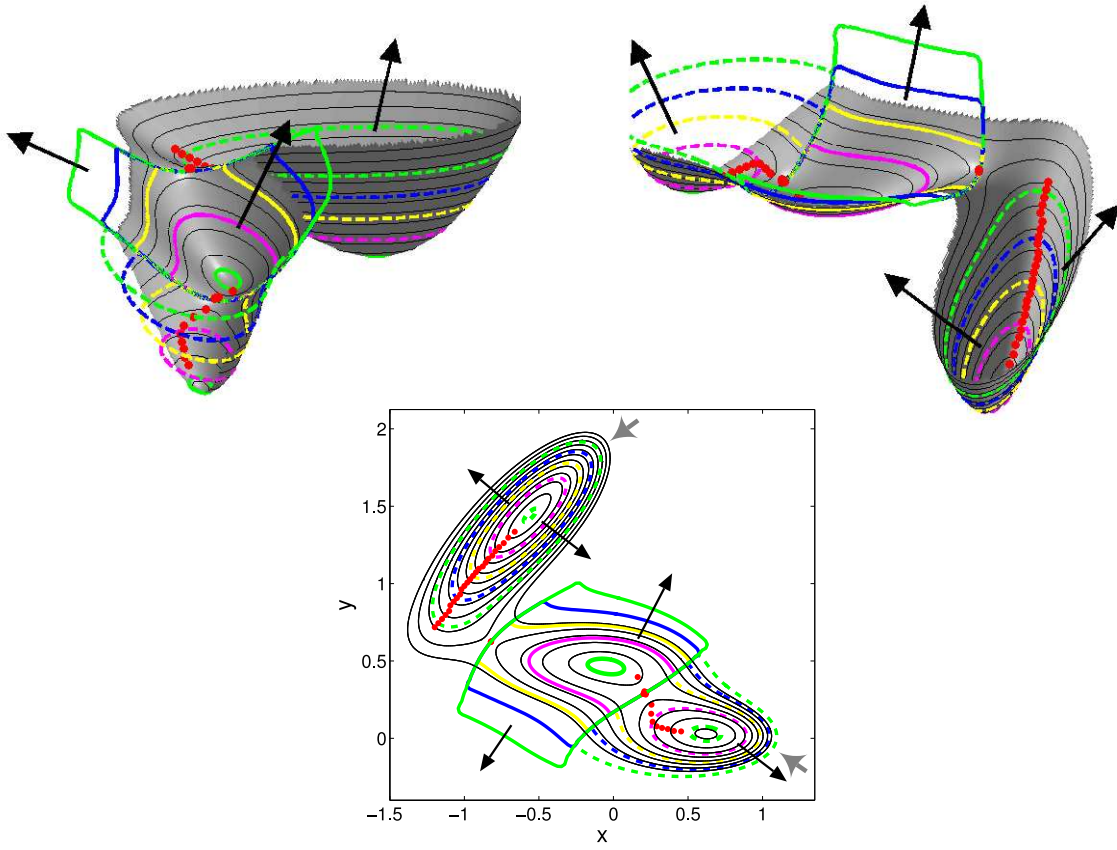


Figure 11

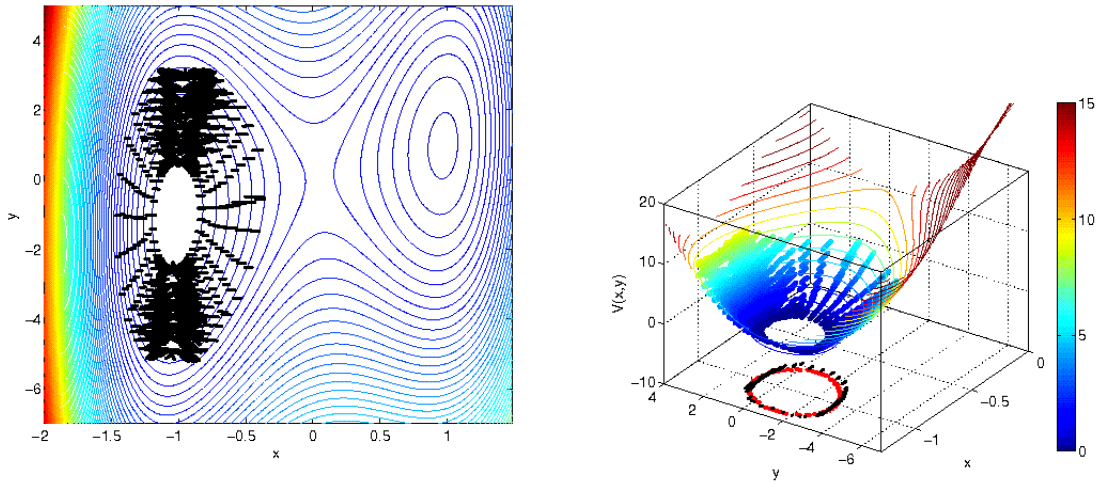


Figure 12

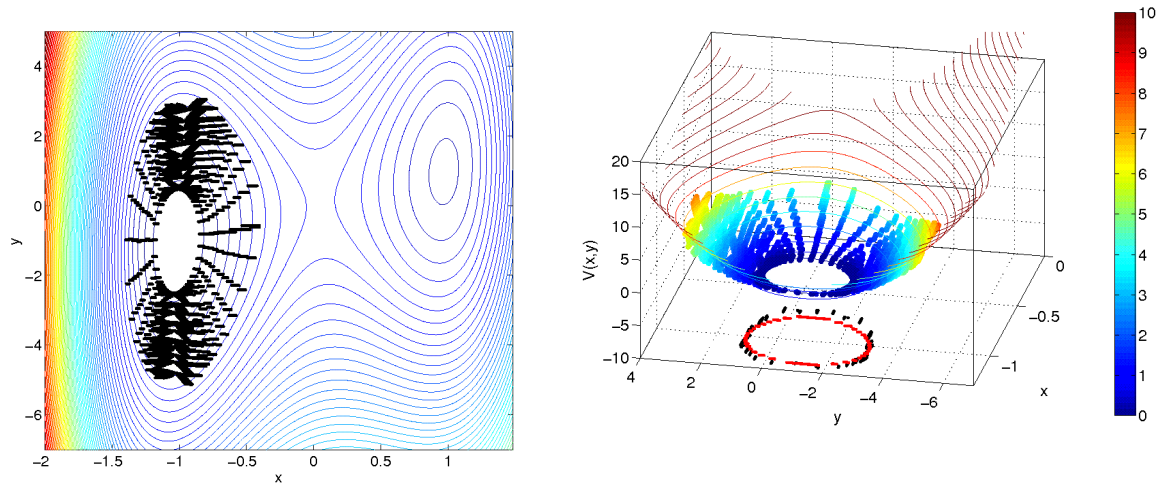


Figure 13

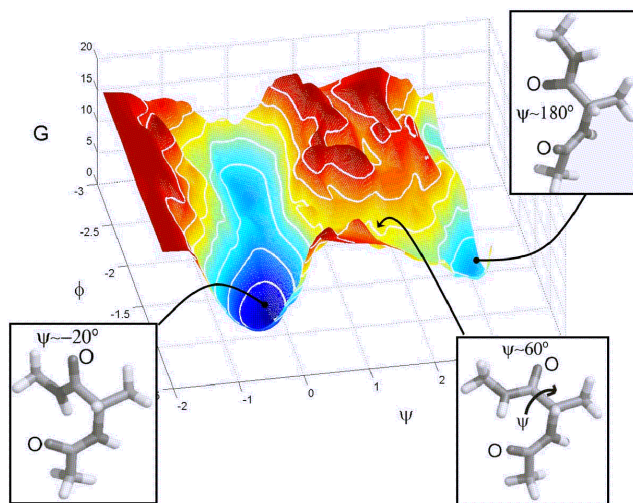


Figure 14

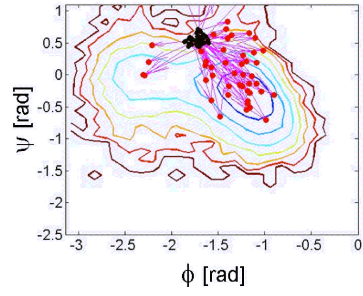
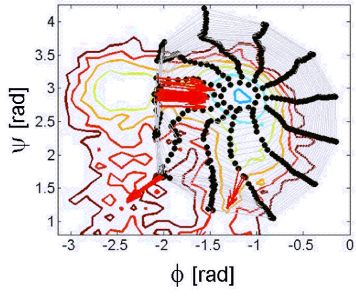


Figure 15



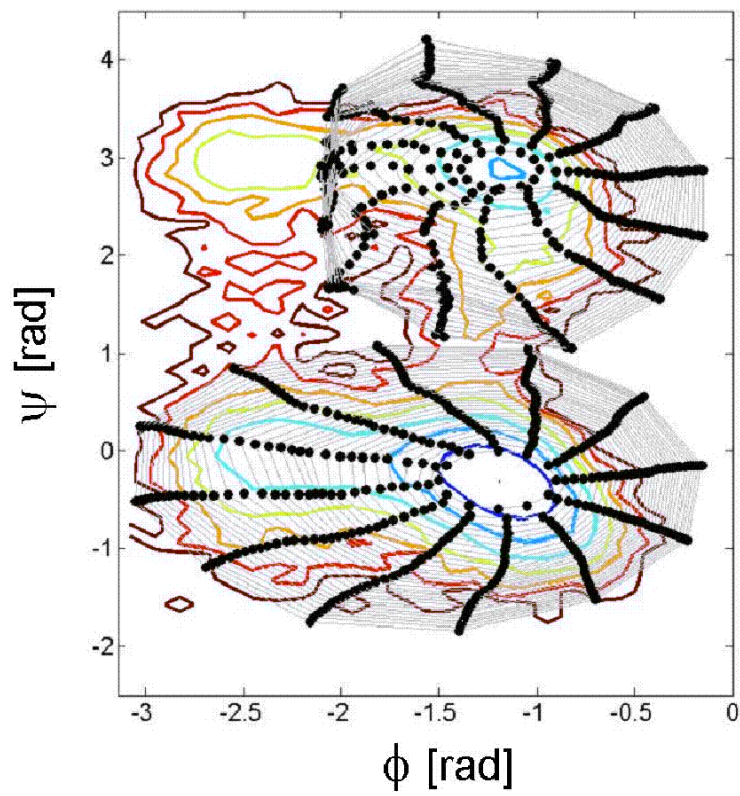


Figure 16